ACS APPLIED MATERIALS & INTERFACES

Research Article

www.acsami.org

MOF-Templated Synthesis of Porous Co_3O_4 Concave Nanocubes with High Specific Surface Area and Their Gas Sensing Properties

Yinyun Lü, Wenwen Zhan, Yue He, Yiting Wang, Xiangjian Kong, Qin Kuang,* Zhaoxiong Xie, and Lansun Zheng

State Key Laboratory of Physical Chemistry of Solid Surfaces & Department of Chemistry, College of Chemistry and Chemical Engineering, Xiamen University, Xiamen, Fujian 361005, China

Supporting Information

ABSTRACT: Porous metal oxides nanomaterials with controlled morphology have received great attention because of their promising applications in catalysis, energy storage and conversion, gas sensing, etc. In this paper, porous Co_3O_4 concave nanocubes with extremely high specific surface area (120.9 $m^2 \cdot g^{-1}$) were synthesized simply by calcining Co-based metal−organic framework (Co-MOF, ZIF-67) templates at the optimized temperature (300 °C), and the formation mechanism of such highly porous structures as well as the influence of the calcination temperature are well explained by taking into account thermal behavior and intrinsic structural features of the Co-MOF precursors. The gas-sensing properties of the as-synthesized porous Co_3O_4 concave nanocubes were systematically tested towards volatile organic compounds including ethanol, acetone, toluene, and benzene. Experimental results reveal that the porous Co_3O_4 concave nanocubes present the highest sensitivity to ethanol with fast response/recovery time (< 10 s) and a low detection limit (at least 10 ppm). Such outstanding gas sensing performance of the porous Co_3O_4 concave nanocubes benefits from their high porosity, large specific surface area, and remarkable capabilities of surface-adsorbed oxygen.

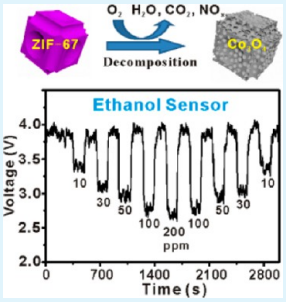

KEYWORDS: *metal-organic frameworks, self-sacrificial template synthesis, porous structure, Co_3O_4, gas sensor*

1. INTRODUCTION

The synthesis of porous metal oxides is always a hot issue in the field of nanomaterials because of their unique advantages, such as large specific surface area and abundant active sites for reactions, fast interfacial transport between adjacent crystallites, and efficient light trapping and utilization arising from pore-induced multireflections.[1−4] Among the present diverse synthetic strategies,[5−8] the self-sacrificial template strategy based on thermolysis of solid precursors is regarded as the most attractive one in fabricating porous nanostructures due to its high effectiveness and low cost. For acquiring porous metal oxides with high surface area, the right template material is the key, because the precursor used as self-sacrificial templates must be able to release large amounts of gases (such as H_2O or CO_2) in the transformation process and also possess comparable structural stability so as to produce massive pores inside the products with preserving the original stereoscopic structure.

Metal-organic frameworks (MOFs) are a class of organic-inorganic hybrid functional materials with high porosity and large specific surface area, and noticeably their pore size and morphology can be easily tuned upon selection of different metal ions and organic bridging ligands.[9,10] Recently, MOFs are proved to be ideal sacrificial templates for fabricating porous metal oxides or carbon nanostructures via thermal decomposition under controlled atmospheres, since the porosity and long-range ordering of MOFs can offer a fast and convenient access for incoming and leaving small molecules and ions in the transformation process.[11−16] In this MOFs templated solid−solid transformation process, noticeably, calcination conditions (e.g., temperature and atmosphere) significantly influence the structure and composition of as-obtained porous products. In this aspect, unfortunately, it is still a lack of insightful and systematic study.

Spinel cobalt oxide (Co_3O_4) is one of the most intriguing magnetic p-type semiconductors and has been widely applied as heterogeneous catalysts,[17,18] electrode materials in supercapacitors and lithium-ion battery,[19−22] and gas sensing materials.[23−25] It is well known that gas sensing is actually a gas-induced resistance response process that happens on the surface of semiconductor materials. Consequently, the most effective method to enhance gas sensing performance is increasing the specific surface area of the sensing materials. Up till now, various Co_3O_4 porous nanostructures, including nanospheres, nanotubes, nanorods, and flowers, have been synthesized by thermal decomposition of Co-based carbonates, hydroxides, coordination complex, and MOFs (e.g., Prussian blue analogues).[21,26−33] Admittedly, specific surface areas of the obtained porous Co_3O_4 products are remarkably enlarged relative to solid particles; nevertheless, most of them are less than 50 $m^2 \cdot g^{-1}$, far below what we expected. Most seriously, some formed porous Co_3O_4 products fail to maintain the original morphologies of the precursor template, probably due to a lack of suitable template and optimal synthetic conditions.[31−33] On the other hand, it is very important to

Received: December 18, 2013
Accepted: February 21, 2014
Published: February 21, 2014

Scheme 1. Schematic Illustration of the Porous Co_3O_4 Concave Nanocubes via a Co-MOFs Templated Transformation Route

avoid the aggregation of Co_3O_4 nanoparticles as sensing materials or catalytsts in practical application environment, such as at high temperature. So it still remains a great challenge to synthesize porous Co_3O_4 with specific morphology and high specific surface area.

In this study, high-purity porous Co_3O_4 concave nanocubes with extremely high specific surface area (120.9 $m^2 \cdot g^{-1}$) were successfully fabricated by calcining Co-based MOFs (Co-MOF, ZIF-67) at an optimized temperature. The influence of the calcination temperature on the porous structure of the as-prepared Co_3O_4 products was detailedly investigated by electron microscopy, nitrogen gas adsorption-desorption, and Raman spectra techniques. Structurally, the concave morphology of the obtained Co_3O_4 porous particles will effectively avoid possible aggregation in practical application. Excitingly, such highly porous Co_3O_4 concave nanocubes were demonstrated to present remarkable sensing performance in detecting volatile organic compounds (VOCs), especially to ethanol.

2. EXPERIMENTAL SECTION

2.1. Chemicals. Cobalt nitrate hexahydrate ($Co(NO_3)_2 \cdot 6H_2O$, 99%), 2-methylimidazole (mIM, 99%), ethanol (99.7%), acetone (99.5%), toluene (99.5%), and benzene (99.5%) were purchased from commercial suppliers (Alfa Aesar and Sinopharm Chemical Regent Co., Ltd.). All the reagents were used without further purification.

2.2. Synthesis of Samples. Porous Co_3O_4 concave nanocubes were prepared via a two-step route, involving the fabrication of Co-MOF (ZIF-67) concave nanocubes and the subsequent calcination treatment at 300 °C (Scheme 1). In the first step, the ZIF-67 concave nanocubes as precursors were prepared via a simple precipitation reaction in aqueous solution at room temperature according to a previous report.[34] Typically, a 3 mL aqueous solution of $Co(NO_3)_2 \cdot 6H_2O$ (0.45 g, 1.55 mmol) was mixed with a 20 mL aqueous solution of 2-methylimizole (5.5 g, 67.1 mmol) and then was stirred for 6 h at room temperature (RT). The resulting purple precipitates were collected by centrifugation, washed with alcohol for 3 times, and dried at 80 °C for 24 h. In the second step, the as-prepared Co-MOF (ZIF-67) precursors were loaded in a ceramic crucible and then heated to 300 °C with a heating rate of 5 °C·min^{-1}. After a calcination treatment in air at 300 °C for 3 h, the purple precursor was finally converted into the black powder. To find the key factor for the formation mechanism of porous concave nanocubes, synthetic experiments with different calcination temperatures from 300 °C to 350 °C and 400 °C was carried out, and the resulting products were denoted as Co_3O_4-300, Co_3O_4-350, and Co_3O_4-400, respectively.

2.3. Characterization of Samples. The morphologies of the products were observed by scanning electron microscopy (SEM, Hitachi S4800) and transmission electron microscopy (TEM, JEOL 2010F) at an accelerating voltage of 200 kV. The composition of the products was determined by X-ray powder diffraction (XRD) recorded on a Rigaku D/max X-ray diffractometer (Cu Kα radiation, λ = 0.15418 nm). The thermogravimetry-differential scanning calorimetry (TG-DSC) curves of the Co-MOF precursors were measured by using SDT Q600TGA thermal gravimetric analyzer under air atmosphere in the temperature range of 30−600 °C with a heating rate of 10 °C·min^{-1}. The specific surface area of the products was measured by the Brunauer-Emmett-Teller (BET) method using nitrogen adsorption and desorption isotherms on a Micromeritics Instrument Corporation sorption analyzer (TriStar II 3020). The pore size and size distribution of the products were calculated by the Barrett−Joyner−Halenda (BJH) method. X-ray photoelectron spectroscopy (XPS) was measured on a Perkin-Elmer model PHI 5600 XPS system from a monochromatic aluminum anode X-ray source with Kα radiation (1486.6 eV), and the spectra were calibrated with the C1s peak at 284.6 eV as an internal standard. Raman spectra were measured on a Renishaw 2000 laser Raman microscope with an argon ion laser with excitation of 514.5 nm. The laser power is 20 mW, and the spot size is 2 mm.

2.4. Gas-Sensing Measurement of Samples. The gas-sensing measurements of the as-prepared porous Co_3O_4 samples were carried out on a WS-30A sensor measurement system (Zhengzhou Winsen Electronics Technology, China). The detailed fabrication and testing processes of the sensors were shown as follows. First, a proper amount of the porous Co_3O_4 sample was mixed with several drops of ethanol, and the resulting paste was coated onto a ceramic tube that was premounted with gold electrodes and platinum conducting wires. An alloy filament was put through the ceramic tube and used as a heater, which can provide the operating temperature from 150 °C to 400 °C by tuning the heating voltage. After the ceramic tube was welded onto a pedestal with six probes, the as-fabricated sensor was finally plugged into a measurement board of the sensor measuring system. Before testing, the sensor was aged in air for 24 h at 300 °C to achieve the device stabilization. After that, the detected gas (ethanol, acetone, benzene, or toluene) was introduced by injecting a certain volume of liquid analytes with a microsyringe onto a metal-plate heater in the test chamber, and the concentrations of the detected gas were calculated according to the total volume (27 L) of gas chamber. The dynamic sensing tests were carried out by repeatedly exposing the sensors to the detected gas in closed chamber and to air by opening the chamber. The resistances of the sensors were measured under a bias voltage of 5 V. The gas-sensing sensitivity of sensors are defined as the ratio R_{gas}/R_{air}, where R_{gas} and R_{air} are the electrical resistance of the sensor in the tested gas and in air at the operating temperature, respectively. In our measurement system, R_{gas} and R_{air} were determined by $R_{air} = (V_c/V_{air} - 1)R_L$ and $R_{gas} = (V_c/V_{gas} - 1)R_L$, where V_{gas} and V_{air} are the output voltage of the sensor in the tested gas and in air at the operating temperature, V_C is the operating voltage of the sensor, and R_L is the load resistance in measurement. Response time and recovery time are defined as the time needed for 90% of total resistance change on exposure to gas and air, respectively.

3. RESULTS AND DISCUSSION

3.1. Morphology and Structure of the Porous Co_3O_4 Concave Nanocubes Transformed from the Co-MOFs Template. Porous Co_3O_4 concave nanocubes with high specific surface area were prepared via a solid chemical transformation from the Co-MOF (ZIF-67) precursors with a calcination treatment at 300 °C for 3 h, as illustrated in Scheme 1. Typical morphology of the Co-MOF precursors is shown in Figure 1a. It can be seen that the Co-MOF precursors are composed of high-purity (>90%) polyhedral particles with an average size of 200 nm. Close-up views reveal that these polyhedra are actually cubic particles with the faces or the edges concave (see insets of Figure 1a). By calcining the Co-MOF precursors at 300 °C for 3 h, a fluffy black powder (i.e., Co_3O_4-300) was obtained, and the typical morphology is presented in

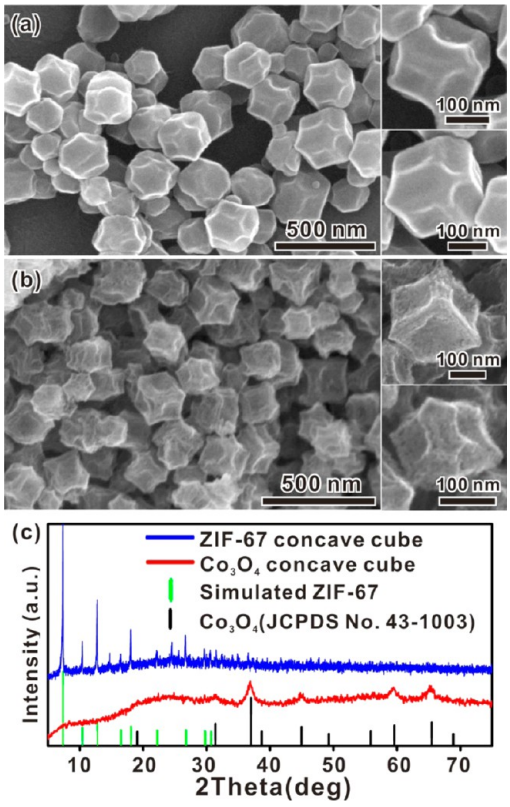

Figure 1. Typical SEM images of (a) the Co-MOF (ZIF-67) concave nanocubes and (b) the porous Co_3O_4 concave nanocubes (i.e., Co_3O_4-300) obtained by calcination at 300 °C for 3 h. Right insets are close-up views of particles in different orientations to show structural details. (c) XRD patterns of the Co-MOF (ZIF-67) concave nanocubes and the Co_3O_4-300 porous concave nanocubes.

Figure 1b. Obviously, the calcined particles retain the similar size (~200 nm) and shape (concave cubes) as the Co-MOF precursors. Compared to the Co-MOF precursors, however, the surface of the particles becomes fairly rough. High-magnification SEM images (inset of Figure 1b) show that these particles are decorated with numerous tiny holes. The corresponding powder XRD patterns (Figure 1c) reveal that the composition of the Co-MOF precursors is ZIF-67, a zeolitic imidazolate framework material of sodalite topology with a unit cell containing two 2-methylimidazole linkers per cobalt ($Co(mIM)_2$), while the calcined product Co_3O_4-300 is composed of pure spinel-type Co_3O_4 (JCPDS Card No. 43-1003), without any impurity phases like Co, CoO, Co_2O_3, and $Co(OH)_2$. Note that all the diffraction peaks of the product are significantly broaden in width and weaken in intensity. This suggests that the as-obtained Co_3O_4-300 concave nanocubes are essentially constructed with a large number of nanosized primary crystallites. In addition, the elemental analysis of Co_3O_4-300 reveals that the content of residual organic ingredients (see Table S1) was only 5.3%, indicating that the overwhelming majority of Co-MOF precursors have decomposed into Co_3O_4.

More structural information of the Co_3O_4-300 porous concave nanocubes was revealed by TEM characterization. As shown in Figure 2a, the projection profiles of most particles remain square with the edges concave, agreeing well with the concave cubic morphology in the SEM observation. The brighter contrast in the center region of squares indicates that

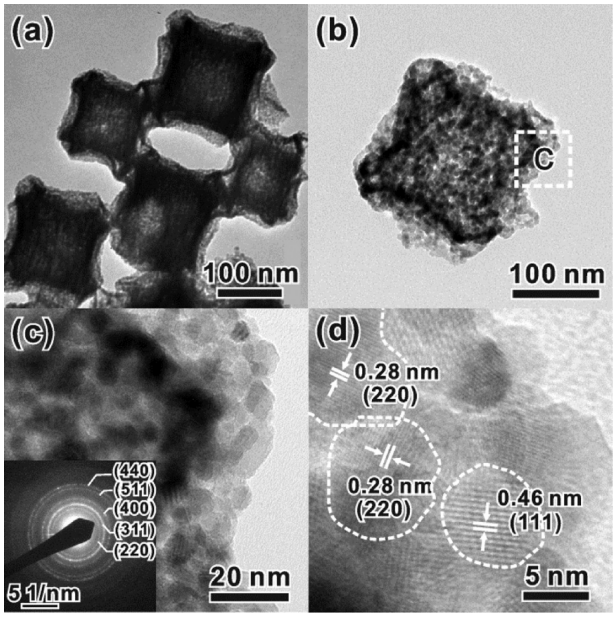

Figure 2. (a) Low-magnification TEM image of the Co_3O_4-300 concave nanocubes obtained by calcination at 300 °C. (b) Low-magnification TEM image of an individual Co_3O_4 concave nanocube. (c) High-magnification TEM image and (d) HRTEM image of the zone "c" in (b). Inset in (c) is the SAED pattern recorded from the whole particle.

the cubic particles are extremely porous in the interior. More clear structural details can be seen in TEM images of cubic particles in different orientations (see Figure S1). A close survey on an individual Co_3O_4 concave nanocube (Figure 2b,c) shows that these concave nanocubes are really composed of numerous primary crystallites of 5−8 nm in size, whereby a large number of pores with about 2−4 nm in size are left between adjacent crystallites. The selected area electronic diffraction (SAED) pattern recorded from the whole porous concave nanocube (inset of Figure 2c) presents a series of concentric rings, indicating that the primary crystallites are randomly attached with each other. As evidence, the high-resolution TEM (HRTEM) image (Figure 2d) shows that these primary crystallites are attached with each other in various orientations, despite displaying clear lattice fringes.

3.2. Influence of the Calcination Temperature on the Formation of the Porous Co_3O_4 Concave Nanocubes. On the basis of the above results, it can be concluded that the products obtained by calcining the Co-MOF precursors at 300 °C are highly porous Co_3O_4 concave nanocubes built with numerous nanocrystallites. In this synthetic method, choosing the appropriate calcination temperature is extremely important, which can ensure that large numbers of pores are generated inside the final Co_3O_4 product while retaining the concave cubic morphology. Our experiments demonstrate that the transformation reaction cannot proceed at calcination temperature below 300 °C. When the calcination temperature of the Co-MOF precursors is raised to 350 °C, the porous concave cubic particles are still achieved, but quite a few of them have collapsed (Figure 3a). When the calcination temperature is raised to 400 °C, the concave cubic morphology of particles entirely disappears, and most of them become quasi-spherical agglomerates (Figure 3b). Besides, the primary crystallite size of the obtained porous particles significantly increases with the increase of the temperature, as shown in the corresponding

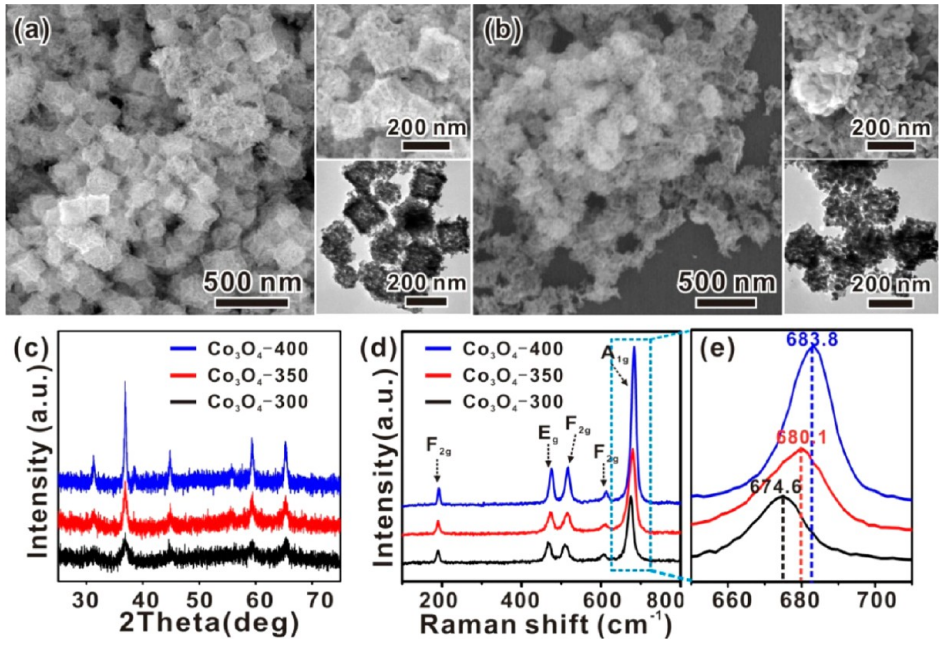

Figure 3. Low-magnification and high-magnification SEM images (top right insets) and TEM images (lower right insets) of (a) the Co_3O_4-350 and (b) Co_3O_4-400 samples obtained after calcination at 350 °C and 400 °C for 3 h. (c) XRD patterns of the three porous Co_3O_4 products prepared at different temperatures. (d) Raman spectra of the three porous Co_3O_4 products and (e) corresponding high-resolution Raman spectra of the A_{1g}-active peaks.

Table 1. Structural Information of the Porous Co_3O_4 Products Synthesized at Different Temperatures

		primary crystallite sizes (nm)		pore size (nm)		
samples	reaction temp (°C)	TEM	XRD	TEM	BJH	specific surface area ($m^2 \cdot g^{-1}$)
Co_3O_4-300	300	5−8	7	2−4	3.6	120.9
Co_3O_4-350	350	14−16	15	13−15	14.2	55.1
Co_3O_4-400	400	26−28	27	29−32	30.7	22.6

TEM images (see insets of Figure 3a-b and Table 1). Accordingly, the size of pores between crystallites increases from 2−4 nm for Co_3O_4-300 to 13−15 nm for Co_3O_4-350 and 29-32 nm for Co_3O_4-400. This structural change is reflected in the XRD patterns of the products. As shown in Figure 3c, the higher the calcination temperature, the narrower the peak width and the stronger the peak intensity. This means that the primary crystallites in the products turn bigger in size and the crystallinity becomes better as the calcination temperature increases. According to the Scherrer equation, the average crystallite size of the Co_3O_4-350 and Co_3O_4-400 samples obtained at 350 and 400 °C are estimated to be 15 and 27 nm, much larger than that (7 nm) of the Co_3O_4-300 sample, which is consistent with the observed values from TEM. The above structural details of all three samples are summarized in Table 1.

Interestingly, the size change in the primary crystallites has a great influence on Raman spectra of the samples. As shown in Figure 3d, all the three porous Co_3O_4 samples present five Raman peaks in the wavenumber range of 100−800 cm^{-1}, corresponding to five Raman-active modes (A_{1g}, E_g, and 3 F_{2g}) of spinel Co_3O_4.[35] For the Co_3O_4-300 porous concave nanocubes, the five Raman peaks locate at 187.8, 468.9, 509.2, 606.7, and 674.6, respectively, which shift to lower wavenumbers by 6−16 cm^{-1} compared to the literature value of bulk Co_3O_4 (see Table 2 for details).[35] Furthermore, an obvious blue shift is observed on all the Raman peaks of the three samples with increasing the calcination temperature.

Table 2. Raman Shifts of the Characteristic Peaks of the Porous Co_3O_4 Products Obtained at Different Calcination Temperatures

		wavenumber (cm^{-1})		
phonon mode	Co_3O_4-300	Co_3O_4-350	Co_3O_4-400	lit. value[35]
F_{2g}	187.8	189.6	191.4	194.4
E_g	468.9	472.4	474.4	482.4
F_{2g}	509.2	514.7	516.6	521.6
F_{2g}	606.7	610.3	612.2	618.4
A_{1g}	674.6	680.1	683.8	691.0

Typically, the strongest peak assigned to the A_{1g}-active mode shifts from 674.6 cm^{-1} (Co_3O_4-300) to 680.1 cm^{-1} (Co_3O_4-350) and 683.8 cm^{-1} (Co_3O_4-400), as shown in Figure 3e. The observed Raman shift towards lower wavenumbers relative to bulk Co_3O_4 should be attributed to the enhanced strain in nanosized primary crystallites of the porous Co_3O_4 particles. Compared with Co_3O_4 single crystals, the primary crystallites of the porous Co_3O_4 concave nanocubes should be much smaller in size, thereby experiencing stronger strain. As a result, a larger Raman shift of the highest-frequency nonpolar mode towards lower wavenumbers takes place with the decreasing crystallite size.[36,37]

To evaluate the specific surface area and the porosity of the Co_3O_4-300 concave nanocubes and the other two products obtained at higher temperatures, the N_2 adsorption−desorption isotherms and BJH pore size distribution analysis were further

performed (Figure 4). The specific surface areas of Co_3O_4-300, Co_3O_4-350, and Co_3O_4-400 are calculated by the BET method

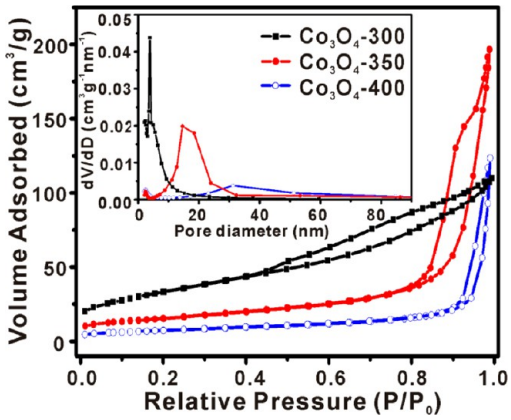

Figure 4. N_2 adsorption-desorption isotherms and pore size distributions of the porous Co_3O_4 products obtained at different calcination temperatures.

to be 120.9, 55.1, and 26.6 $m^2 \cdot g^{-1}$, respectively. Remarkably, the specific surface area of Co_3O_4-300 is far higher than most of the previously reported porous Co_3O_4 nanostructures,[26−33] and all of the samples display a typical type IV adsorption isotherm with a H3-type hysteresis loop at a relative pressure of 0.4−1.0 for Co_3O_4-300, 0.8−1.0 for Co_3O_4-350, and 0.9−1.0 for Co_3O_4-400, indicating the presence of the mesoporous structure.[38] Along with the calcination temperature increasing, a shift of adsorption step and hysteresis loop toward higher relative pressure is observed, which indicates that the pore size of the synthesized Co_3O_4 product increases. The following abrupt increase in the curves of Co_3O_4-350 and Co_3O_4-400 at high relative pressure (above 0.9) can be ascribed to multilayer adsorption of nitrogen in the macropores formed among the resultant Co_3O_4 particles. Such difference in the isotherm shapes of the three samples suggests that there are significant differences in the pore structures of these samples. This deduction is further substantiated by the results of pore size distribution measurements (insets of Figure 4). For the Co_3O_4-300 sample, the appearance of one sharp peak at about 3.6 nm indicates that the pore size of Co_3O_4-300 is comparatively uniform. When it comes to the temperature of 350 °C, the pore size distribution has a relatively wide peak centered at 14.2 nm, suggesting that the pores of Co_3O_4-350 become larger in size and wider in distribution. With the calcination temperature increasing to 400 °C, the pore size distribution of the products reveals a fairly wide distribution centered at 30.7 nm. The pore size distribution results are well consistent with TEM observations (see Table 1 for details). It should be easily understood that the crystallite size has a significant growth through solid-state diffusion and coalescence with the calcination temperature increasing, thereby leading to the decrease of the specific surface areas and the increase of the pore sizes.

As described above, the crystallite size of the porous Co_3O_4 products would increase at excessive calcination temperature, and, worse, the porous concave structure is hardly maintained. These structural changes are closely related to thermal stability of the Co-MOF precursors as well as their intrinsic structural features, such as high porosity, large pore volume, and low content of metal ions. According to the thermal gravimetric analysis (the black curve in Figure 5a), the Co-MOF (ZIF-67) precursors are highly stable up to 300 °C where they begin to decompose. As the temperature rises to around 350 °C, the weight loss drops sharply and finally flattens at about 390 °C, where an obvious exothermic peak can be seen in the corresponding DSC curve (the dotted blue curve in Figure 5a). The total weight loss in the decomposition process from 300 °C to 390 °C is ~62.5%, which well agrees with the weight change in the transformation from ZIF-67 to Co_3O_4. Such a large weight loss means that large amounts of H_2O, CO_2, and NO_x will be released in the decomposing process of the Co-MOF precursors. More importantly, MOFs like ZIF-67 possess high porosity and large pore volume, so that the mass-to-volume ratio of metal ions is very low. This means that a large structural strain will be produced in the transformation process from ZIF-67 to Co_3O_4.

When combining these intrinsic structural features with thermal decomposition behavior of Co-MOFs, the influence of the calcination temperature on the morphology and structure of the final porous Co_3O_4 products is easy to understand. As schematically illustrated in Figure 5b, when the calcination temperature reaches and exceeds the decomposition temperature of the precursor, organic ligands and other guest molecules in the Co-MOF concave nanocube precursors are burned out in air atmosphere and released in the form of CO_2, H_2O, and NO_x, while Co(II) ions in the precursors react with O_2 to form new porous Co_3O_4 frameworks. At the decomposition temperature of the precursor (i.e., 300 °C), the decomposition process is comparatively slow, thereby forming small Co_3O_4 crystallites, but it thoroughly completes once the precursors are calcined long enough. With the calcination temperature increasing, the Co atoms migrate faster so as to form the bigger Co_3O_4 crystallites in the transformation

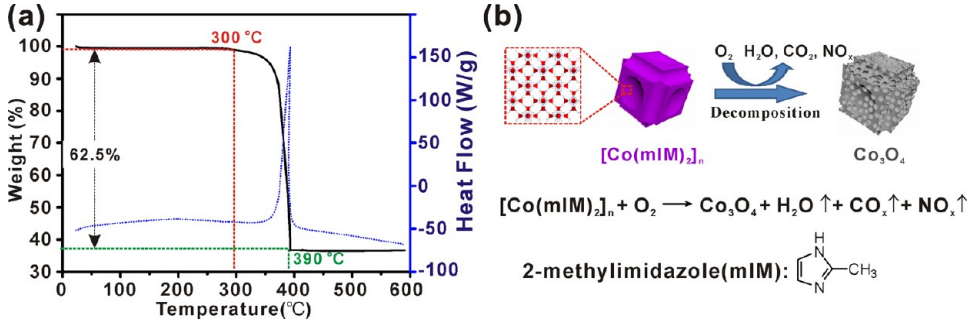

Figure 5. (a) TG-DSC curves of the Co-MOF (ZIF-67) precursor. (b) Schematic illustration of the formation of Co_3O_4 porous concave nanocubes via the Co-MOF (ZIF-67)-templated chemical transformation.

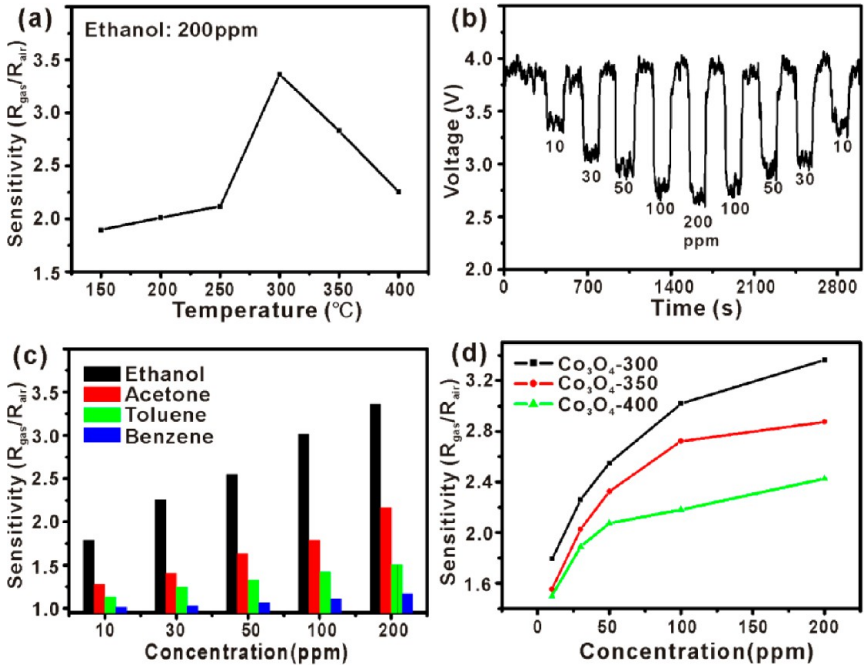

Figure 6. (a) Operating temperature-dependent sensitivity curve of the Co_3O_4-300 sensor (i.e. porous concave nanocubes) in the presence of 200 ppm ethanol. (b) Dynamic sensing curve of the Co_3O_4-300 sensor in the presence of ethanol with different concentrations. (c) Comparison between concentration-dependent sensitivities of the Co_3O_4-300 sensor with regard to different gases. (d) Concentration-dependent sensitivity curves of the porous Co_3O_4 product obtained at different calcination temperatures.

process. To reduce the accumulating structural strain, the formed porous structures have to shrink and finally collapse into quasi-spherical particles. On the other hand, the H_2O, CO_2, and NO_x gases produced from thermal decomposition would be released in a faster rate at higher calcination temperatures, severely destroying the structure integrity of the Co_3O_4 products. Thus it can be deduced that the optimal calcination temperature for the MOF-templated transformation process is the initial decomposition temperature of the MOF precursors (e.g., 300 °C for ZIF-67), whereby the porosity of the products is maximized and the structure damage is minimized.

Noticeably, in addition to the calcination temperature, the calcination atmosphere also significantly influences the structure of as-obtained porous products in MOFs templated solid−solid transformation process. As shown in Figure S2, the obtained product was mainly composed of quasi-spherical agglomerates when the transformation process proceeded in N_2 atmosphere. Because of lacking enough O_2, the Co^{2+} ions in the ZIF-67 precursors are hardly transformed into Co_3O_4 in N_2 or other inactive gases, so that the structure will be seriously destroyed by the released gases during the calcilation process.

3.3. Enhanced Gas-Sensing Performance of the Porous Co_3O_4 Concave Nanocubes. Based on the above analysis, providing the appropriate calcination temperature, the MOFs-templated transformation strategy is indeed highly effective in fabricating porous metal oxide nanomaterials like Co_3O_4 with high specific surface area. Predictably, such highly porous structure and large specific surface area of the formed products are bound to greatly enhance their surface-related properties such as gas sensing. As a typical p-type semiconductor, Co_3O_4 has been demonstrated to have a promising application in gas sensing.[23−25] The gas-sensing mechanism of Co_3O_4 essentially belongs to the surface-resistance controlled mode. When a p-type Co_3O_4-based sensor is exposed to a reducing gas (such as ethanol), the reducing gas molecules will interact with preadsorbed oxygen on the surface of the sensor and release free electrons to the bulk, and then the released electrons neutralize the hole carriers in Co_3O_4, thereby leading to the increase of the resistance (R_{gas}). Considering $R_{gas} = (V_C/V_{gas}-1)R_L$ in our measurement system, the increase of the resistance manifests the decrease of the output voltage (V_{gas}).

For evaluating the performance of Co_3O_4-300 porous concave nanocubes as sensing materials, ethanol was chosen as a target analyte because of its well established sensing mechanism and wide application in our everyday life and production. In order to find the optimal operating temperature, the sensing of the Co_3O_4-300 sensor to 200 ppm of ethanol gas was measured at different operating temperatures ranging from 150 to 400 °C. As shown in Figure 6a, the response of the Co_3O_4-300 sensor gradually increases to the maximum value at 300 °C and then decreases afterwards with the continuing rise of the operating temperature. The best operating temperature of 300 °C for the Co_3O_4 concave nanocubes sensor is consistent with that of most Co_3O_4 nanostructure-based sensors in the literature.[39−41] The influence of the operating temperature on the sensor response can be explained qualitatively from a dynamic balance between the initial fast adsorption of ethanol molecules and the further acceleration of desorption as the temperature maintains rising.[42] When the operating temperature is too low, the chemical activation of porous Co_3O_4 concave nanocubes is consequently small, leading to a very low response. When the operating temperature increases too much, some adsorbed gas molecules may escape from the sensor surface before reaction due to their enhanced activation, thus the response will decrease correspondingly. Furthermore, the decrease of the sensor response at too high an operating temperature probably results from the reduced gas concentration due to the combustion of the tested gas.[43]

dx.doi.org/10.1021/am405858v | ACS Appl. Mater. Interfaces 2014, 6, 4186−4195

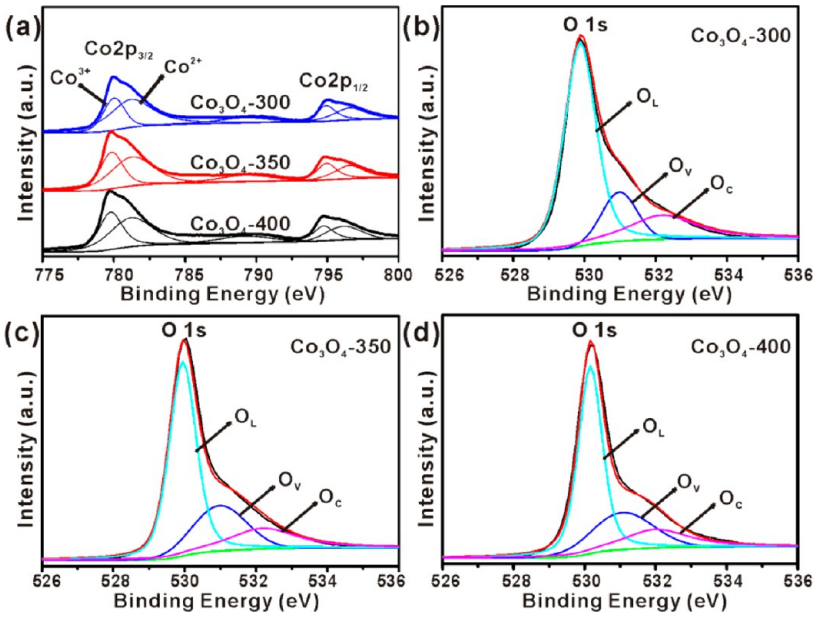

Figure 7. (a) XPS spectra of Co 2p in the porous Co_3O_4 products obtained at different calcination temperatures. XPS spectra and curve-fitting of O 1s in (b) Co_3O_4-300, (c) Co_3O_4-350, and (d) Co_3O_4-400.

Figure 6b shows the dynamic sensing curve of the Co_3O_4-300 sample measured at the optimal operating temperature of 300 °C, which clearly reveals the response-recovery performances of the sensors. The output voltage of the Co_3O_4 sensor decreases abruptly in the presence of ethanol and increases to its initial value when the test chamber is refreshed with air. Noticeably, the Co_3O_4-300 sensor shows a very stable signal with on/off phenomenon when switching between air and ethanol. With increasing the ethanol concentration from 10 ppm to 200 ppm, the on/off voltage response of the sensor increases monotonically. In turn, the voltage response of the sensor decreases when the ethanol concentration is decreased from 200 ppm to 10 ppm again. The above results illustrate that the Co_3O_4-300 sensor could detect ethanol gas in a wide range of concentrations. The minimum concentration of 10 ppm is far lower than the detection limit (200 ppm) imposed for a breath analyzer.[41,44] Besides that, the symmetry of the on/off curves reveals good sensing reproducibility of the Co_3O_4-300 sensor towards ethanol of the same concentration. Note that both response and recovery of the Co_3O_4-300 sensor are very fast, taking less than 10 s. To our knowledge, the response and recovery of the Co_3O_4-300 sensor are much faster than the previously reported Co_3O_4 nanorod arrays (90 s) and Co_3O_4 nanofibers (20 s), which is favorable for the rapid detection of ethanol.[40,44] Considering its extremely porous structure and high specific surface area, the fast response and recovery of the Co_3O_4-300 sensor to ethanol should be attributed to the shortened diffusion path of the analyte molecules to the surface of sensing materials and extremely abundant adsorption sites.[45]

Sensing specificity is another key parameter for gas sensor. Figure 6c compares sensitivities of the Co_3O_4-300 sensors upon exposure to different concentrations of ethanol, acetone, toluene, and benzene, which all are reductive VOCs and thus are similar in the response mechanism. The sensitivity of the sensors for the other three gases increases monotonically with increasing gas concentrations, analogous to ethanol. By contrast, the response of the Co_3O_4-300 sensors to different VOCs follows the order of ethanol ≫ acetone > toluene > benzene. As for the same concentration of gases, the sensitivity for ethanol is 2 times higher than acetone, 4 times than toluene, and 13 times than benzene, respectively. Thus it can be seen that the as-synthesized porous Co_3O_4 concave nanocubes exhibit remarkable selectivity to ethanol. Apparently, the sensitivity of sensors depends upon the chemical nature of gas substances. In the case of organic normal chain compounds (ethanol and acetone), the compounds with highly nucleophilic groups would generate higher sensitivity. For the benzene derivatives (toluene and benzene), the sensor response increases slightly with the increasing number of methyl groups. The effect of substituents of aromatic compounds is too complicated to be explained simply by inductive or mesomeric effect. Aromatic compounds other than halides, however, have been demonstrated to show a good correlation between their dipole moments and response sensitivity. It appears that the larger polarization is, the higher the sensitivity is.[46]

From the above results, it can be seen that the Co_3O_4-300 porous concave nanocubes exhibit high sensitivity, good reproducibility, and high stability in gas sensing, which should be closely associated with their highly porous structure and large specific surface area. To confirm this finding, the concentration-dependent sensitivities of different porous Co_3O_4 samples (i.e., Co_3O_4-300, Co_3O_4-350, and Co_3O_4-400) were systematically compared, and the results are shown in Figure 6d. The sensitivities of all three sensors increase as the gas concentrations. At the same gas concentration, Co_3O_4-300 possesses the highest sensitivity, followed by Co_3O_4-350 and Co_3O_4-400, which is consistent with the order of the three samples in the specific surface areas (120.9 $m^2 \cdot g^{-1}$ for Co_3O_4-300 > 59.1 $m^2 \cdot g^{-1}$ for Co_3O_4-350 > 26.6 $m^2 \cdot g^{-1}$ for Co_3O_4-400, Table 1). For the surface resistance-controlled gas sensors like Co_3O_4, the change of surface electrical resistances is mainly caused by the adsorption and desorption of oxygen species and targeted analytes on the surface of the sensing materials. The larger surface area of sensing materials normally results in the more active sites on the surface for chemical or physical interactions, thereby giving rise to better sensing performance.

Table 3. Results of Curve Fitting of O 1s XPS Spectra of the Different Co_3O_4 Samples

Co_3O_4 samples		Co $2p_{3/2}$	Co $2p_{1/2}$	O_L (Co−O)	O_V (vacancy)	O_C (chemisorbed)
Co_3O_4-300	binding energy (eV)	779.84	794.75	529.88	530.98	532.18
	relative percentage (%)			65.6	14.9	19.5
Co_3O_4-350	binding energy (eV)	779.85	794.79	529.94	530.97	532.18
	relative percentage (%)			58.4	23.1	18.5
Co_3O_4-400	binding energy (eV)	779.89	794.86	530.16	531.06	531.99
	relative percentage (%)			57.9	24.3	17.8

In addition to the specific surface area, the crystallinity of Co_3O_4 can also influence its gas sensing performance. Generally, the crystallinity of a material will increase as the calcination temperature increases, thereby leading to an improved electronic transportation between the primary sensing particles, and consequently the gas sensing performance of the material can be significantly enhanced.[47] Although one may suspect the role of the sample crystallinity here, we have to call attention to the fact that Co_3O_4-350 and Co_3O_4-400 possess lower sensing activity in direct opposition to their better crystallinity than Co_3O_4-300. Therefore the surface area is the dominating factor influencing the sensing activity.

To confirm the influence of the adsorbed oxygen species on the sensing performance of the sensors, the XPS spectra of the three Co_3O_4 products prepared at different temperatures were further measured. Figure 7a shows Co 2p XPS spectra of the samples Co_3O_4-300, Co_3O_4-350, and Co_3O_4-400 for comparison. It is found that the Co 2p XPS peaks of the three Co_3O_4 samples are analogous for their position and distribution. All the XPS spectra present two major peaks at 794.8 eV and 779.8 eV, respectively, corresponding to the Co $2p_{1/2}$ and Co $2p_{3/2}$ spin-orbit peaks of Co_3O_4. Note that a weak satellite peak at 789.8 eV, about 10.0 eV higher than the position of the main peak of Co $2p_{3/2}$, is clearly detected in the spectra, which is an important characteristic for the Co_3O_4 phase.[48]

However, there are some slight differences between O 1s XPS peaks of three Co_3O_4 samples, which are asymmetrical with a visible shoulder at higher binding energy. As shown in Figure 7b-d, each asymmetric O1s peak can be coherently fitted by three nearly Gaussian components. The O_L component of O 1s spectra centered at 530 ± 0.2 eV is attributed to the lattice oxygen in the Co_3O_4 phase, the O_V component at the medium binding energy (531 ± 0.1 eV) is associated with O^{2-} ions in oxygen-deficient regions within the matrix of Co_3O_4 (oxygen vacancies), and the O_C component at around 532 ± 0.2 eV is usually attributed to chemisorbed and dissociated oxygen species (O_2^-, O^{2-}, or O^-) and OH^-.[49,50] Noticeably, the relative percentage of the O_V component increases continuously with the increase of calcination temperature; on the contrary, the relative percentage of the O_C component gradually decreases. The above results clearly indicate the change in the oxygen chemical states is as a result of the calcination temperature. Table 3 summarizes the relative percentage variation of each component on the surface of the Co_3O_4 samples with temperature. The relative percentages of the O_C component in three different samples are about 19.5% (Co_3O_4-300), 18.5% (Co_3O_4-300), and 17.8% (Co_3O_4-400), respectively. Obviously, Co_3O_4-300 with porous concave cubic structures are able to absorb more oxygen species than the other two porous samples, Co_3O_4-350 and Co_3O_4-400. When the excellent chemisorbed ability to oxygen species is coupled with the extremely high specific surface area, it is inevitable that the sensing performance of porous Co_3O_4 concave nanocubes sample would be markedly enhanced .

4. CONCLUSIONS

In summary, highly porous Co_3O_4 concave cubic particles with extremely high specific surface area (120.9 $m^2 \cdot g^{-1}$) were successfully fabricated via a simple Co-MOFs templated chemical transformation at 300 °C. Controlling an appropriate calcination temperature was found to be vital for acquiring these porous structures with high porosity and large specific surface area. Thanks to such large surface area and excellent chemisorbed ability to oxygen species, the as-synthesized porous Co_3O_4 concave nanocubes exhibited remarkable performances in gas sensing, such as high sensitivity, low detection limit (at least 10 ppm), fast response and recovery (within 10 s), and good selectivity to ethanol. Given versatile applications of Co_3O_4, the as-prepared Co_3O_4 porous concave nanocubes are also likely to exhibit outstanding performance in other surface-related applications, for example catalysis, lithium ion battery, supercapacitors, and so on. More importantly, this MOFs-templated synthetic strategy is facilely extended to the fabrication of other porous transition metal oxides with well-defined structures, since we can be supplied with abundant template materials from the MOFs family.

■ ASSOCIATED CONTENT

Supporting Information

Elemental analysis (Table S1), SEM images of Co_3O_4-300 particles in different orientations (Figure S1), and SEM images of the products obtained in N_2 (Figure S2). This material is available free of charge via the Internet at http://pubs.acs.org.

■ AUTHOR INFORMATION

Corresponding Author

*E-mail: qkuang@xmu.edu.cn.

Notes

The authors declare no competing financial interest.

■ ACKNOWLEDGMENTS

This work was supported by the National Basic Research Program of China (2011CBA00508 and 2013CB933901), the National Natural Science Foundation of China (21171142, 21131005, 21333008, and 21371144), and the program for New Century Excellent Talents in University (NCET-11-0294).

■ REFERENCES

(1) Waitz, T.; Wagner, T.; Sauerwald, T.; Kohl, C.-D.; Tiemann, M. Ordered Mesoporous In_2O_3: Synthesis by Structure Replication and Application as a Methane Gas Sensor. *Adv. Funct. Mater.* **2009**, *19*, 653−661.

(2) Kuang, Q.; Yang, S. H. Template Synthesis of Single-Crystal-Like Porous $SrTiO_3$ Nanocube Assemblies and Their Enhanced Photo-

catalytic Hydrogen Evolution. *ACS Appl. Mater. Interfaces* **2013**, *5*, 3683−3690.
(3) Yen, H.; Seo, Y.; Kaliaguine, S.; Kleitz, F. Tailored Mesostructured Copper/Ceria Catalysts with Enhanced Performance for Preferential Oxidation of CO at Low Temperature. *Angew. Chem., Int. Ed.* **2012**, *51*, 12032−12035.
(4) Sayle, T. X. T.; Maphanga, R. R.; Ngoepe, P. E.; Sayle, D. C. Predicting the Electrochemical Properties of MnO_2 Nanomaterials Used in Rechargeable Li Batteries: Simulating Nanostructure at the Atomistic Level. *J. Am. Chem. Soc.* **2009**, *131*, 6161−6173.
(5) Pinna, N.; Niederberger, M. Surfactant-Free Nonaqueous Synthesis of Metal Oxide Nanostructures. *Angew. Chem., Int. Ed.* **2008**, *47*, 5292−5304.
(6) Shi, Y.; Wan, Y.; Zhao, D. Ordered Mesoporous Non-Oxide Materials. *Chem. Soc. Rev.* **2011**, *40*, 3854−3878.
(7) Zheng, X. L.; Kuang, Q.; Yan, K. Y.; Qiu, Y. C.; Qiu, J. H.; Yang, S. H. Mesoporous TiO_2 Single Crystals: Facile Shape-, Size-, and Phase Controlled Growth and Efficient Photocatalytic Performance. *ACS Appl. Mater. Interfaces* **2013**, *5*, 11249−11257.
(8) Lee, J.; Orilall, M. C.; Warren, S. C.; Kamperman, M.; DiSalvo, F. J.; Wiesner, U. Direct Access to Thermally Stable and Highly Crystalline Mesoporous Transition-Metal Oxides with Uniform Pores. *Nat. Mater.* **2008**, *7*, 222−228.
(9) Rowsell, J. L. C.; Yaghi, O. M. Metal−Organic Frameworks: A New Class of Porous Materials. *Microporous Mesoporous Mater.* **2004**, *73*, 3−14.
(10) Tranchemontagne, D. J.; Mendoza-Cortes, J. L.; O'Keeffe, M.; Yaghi, O. M. Secondary Building Units, Nets and Bonding in the Chemistry of Metal−Organic Frameworks. *Chem. Soc. Rev.* **2009**, *38*, 1257−1283.
(11) Peng, L.; Zhang, J.; Xue, Z.; Han, B.; Li, J.; Yang, G. Large-Pore Mesoporous Mn_3O_4 Crystals Derived from Metal−Organic Frameworks. *Chem. Commun.* **2013**, *49*, 11695−11697.
(12) Gai, P.; Zhang, H.; Zhang, Y.; Liu, W.; Zhu, G.; Zhang, X.; Chen, J. Simultaneous Electrochemical Detection of Ascorbic Acid, Dopamine and Uric Acid Based on Nitrogen Doped Porous Carbon Nanopolyhedra. *J. Mater. Chem. B* **2013**, *1*, 2742−2749.
(13) deKrafft, K. E.; Wang, C.; Lin, W. Metal-Organic Framework Templated Synthesis of Fe_2O_3/TiO_2 Nanocomposite for Hydrogen Production. *Adv. Mater.* **2012**, *24*, 2014−2018.
(14) Liu, B.; Shioyama, H.; Akita, T.; Xu, Q. Metal-Organic Framework as a Template for Porous Carbon Synthesis. *J. Am. Chem. Soc.* **2008**, *130*, 5390−5391.
(15) Jacobs, B. W.; Houk, R. J. T.; Anstey, M. R.; House, S. D.; Robertson, I. M.; Talinc, A. A.; Allendorf, M. D. Ordered Metal Nanostructure Self-Assembly Using Metal−Organic Frameworks As Templates. *Chem. Sci.* **2011**, *2*, 411−416.
(16) Bhakta, R. K.; Herberg, J. L.; Jacobs, B.; Highley, A.; Richard Behrens, J.; Ockwig, N. W.; Greathouse, J. A.; Allendorf, M. D. Metal-Organic Frameworks As Templates for Nanoscale $NaAlH_4$. *J. Am. Chem. Soc.* **2009**, *131*, 13198−13199.
(17) Hu, L.; Sun, K.; Peng, Q.; Xu, B.; Li, Y. Surface Active Sites on Co_3O_4 Nanobelt and Nanocube Model Catalysts for CO Oxidation. *Nano Res.* **2010**, *3*, 363−368.
(18) Ren, Y.; Ma, Z.; Qian, L.; Dai, S.; He, H.; Bruce, P. G. Ordered Crystalline Mesoporous Oxides as Catalysts for CO Oxidation. *Catal. Lett.* **2009**, *131*, 146−154.
(19) Wang, B.; Zhu, T.; Wu, H. B.; Xu, R.; Chen, J. S.; Lou, X. W. Porous Co_3O_4 Nanowires Derived from Long $Co(CO_3)_{0.5}(OH)\cdot 0.11H_2O$ Nanowires with Improved Supercapacitive Properties. *Nanoscale* **2012**, *4*, 2145−2149.
(20) Zhu, T.; Chen, J. S.; Lou, X. W. Shape-Controlled Synthesis of Porous Co_3O_4 Nanostructures for Application in Supercapacitors. *J. Mater. Chem.* **2010**, *20*, 7015−7020.
(21) Du, N.; Zhang, H.; Chen, B. D.; Wu, J. B.; Ma, X. Y.; Liu, Z. H.; Zhang, Y. Q.; Yang, D. R.; Huang, X. H.; Tu, J. P. Porous Co_3O_4 Nanotubes Derived From $Co_4(CO)_{12}$ Clusters on Carbon Nanotube Templates: A Highly Efficient Material For Li-Battery Applications. *Adv. Mater.* **2007**, *19*, 4505−4509.
(22) Zhu, J.; Bai, L.; Sun, Y.; Zhang, X.; Li, Q.; Cao, B.; Yan, W.; Xie, Y. Topochemical Transformation Route to Atomically Thick Co_3O_4 Nanosheets Realizing Enhanced Lithium Storage Performance. *Nanoscale* **2013**, *5*, 5241−5246.
(23) Li, W.; Xu, L.; Chen, J. Co_3O_4 Nanomaterials in Lithium-Ion Batteries and Gas Sensors. *Adv. Funct. Mater.* **2005**, *15*, 851−857.
(24) Geng, B.; Zhan, F.; Fang, C.; Yu, N. A Facile Coordination Compound Precursor Route to Controlled Synthesis of Co_3O_4 Nanostructures and Their Room-Temperature Gas Sensing Properties. *J. Mater. Chem.* **2008**, *18*, 4977−4984.
(25) Li, C. C.; Yin, X. M.; Wang, T. H.; Zeng, H. C. Morphogenesis of Highly Uniform $CoCO_3$ Submicrometer Crystals and Their Conversion to Mesoporous Co_3O_4 for Gas-Sensing Applications. *Chem. Mater.* **2009**, *21*, 4984−4992.
(26) Xiong, S.; Chen, J. S.; Lou, X. W.; Zeng, H. C. Mesoporous Co_3O_4 and CoO@C Topotactically Transformed from Chrysanthemum-Like $Co(CO_3)_{0.5}(OH)\cdot 0.11H_2O$ and Their Lithium-Storage Properties. *Adv. Funct. Mater.* **2012**, *22*, 861−871.
(27) Li, C. C.; Yin, X. M.; Li, Q. H.; Chen, L. B.; Wang, T. H. Topochemical Synthesis of Cobalt Oxide-Based Porous Nanostructures for High-Performance Lithium-Ion Batteries. *Chem. - Eur. J.* **2011**, *17*, 1596−1604.
(28) Nguyen, H.; El-Safty, S. A. Meso- and Macroporous Co_3O_4 Nanorods for Effective VOC Gas Sensors. *J. Phys. Chem. C* **2011**, *115*, 8466−8474.
(29) Zhang, F.; Hao, L.; Zhang, L.; Zhang, X. Solid-State Thermolysis Preparation of Co_3O_4 Nano/Micro Superstructures From Metal-Organic Framework for Supercapacitors. *Int. J. Electrochem. Sci.* **2011**, *6*, 2943−2954.
(30) Yan, N.; Hu, L.; Li, Y.; Wang, Y.; Zhong, H.; Hu, X.; Kong, X.; Chen, Q. Co_3O_4 Nanocages for High-Performance Anode Material in Lithium-Ion Batteries. *J. Phys. Chem. C* **2012**, *116*, 7227−7235.
(31) Das, R.; Pachfule, P.; Banerjee, R.; Poddar, P. Metal and Metal Oxide Nanoparticle Synthesis from Metal Organic Frameworks (MOFs): Finding the Border of Metal and Metal Oxides. *Nanoscale* **2012**, *4*, 591−599.
(32) Liu, B.; Zhang, X.; Shioyama, H.; Mukai, T.; Sakai, T.; Xu, Q. Converting Cobalt Oxide Subunits in Cobalt Metal-Organic Framework into Agglomerated Co_3O_4 Nanoparticles As an Electrode Material for Lithium Ion Battery. *J. Power Sources* **2010**, *195*, 857−861.
(33) Meng, F.; Fang, Z.; Li, Z.; Xu, W.; Wang, M.; Liu, Y.; Zhang, J.; Wang, W.; Zhao, D.; Guo, X. Porous Co_3O_4 Materials Prepared by Solid-State Thermolysis of a Novel Co-MOF Crystal and Their Superior Energy Storage Performances for Supercapacitors. *J. Mater. Chem. A* **2013**, *1*, 7235−7241.
(34) Qian, J.; Sun, F.; Qin, L. Hydrothermal Synthesis of Zeolitic Imidazolate Framework-67 (ZIF-67) nanocrystals. *Mater. Lett.* **2012**, *82*, 220−223.
(35) Hadjievl, V. G.; Ilievl, M. N.; Vergilov, I. V. The Raman Spectra of Co_3O_4. *J. Phys. C: Solid State Phys.* **1988**, *21*, 199−201.
(36) Zhou, H.; Chen, L.; Malik, V.; Knies, C.; Hofmann, D. M.; Bhatti, K. P.; Chaudhary, S.; Klar, P. J.; Heimbrodt, W.; Klingshirn, C.; Kalt, H. Raman Studies of ZnO:Co Thin Films. *Phys. Status Solidi A* **2007**, *204*, 112−117.
(37) Nemanich, R.; Solin, S.; Martin, R. Light Scattering Study of Boron Nitride Microcrystals. *Phys. Rev. B* **1981**, *23*, 6348−6356.
(38) Michal, K.; Mietek, J. Gas Adsorption Characterization of Ordered Organic-Inorganic Nanocomposite Materials. *Chem. Mater.* **2001**, *13*, 3169−3183.
(39) Choia, K.; Kima, H.; Min, K.; Liub, D.; Caob, G.; Lee, J. C_2H_5OH Sensing Characteristics of Various Co_3O_4 Nanostructures Prepared by Solvothermal Reaction. *Sens. Actuators, B* **2010**, *146*, 183−189.
(40) Yoon, J.-W.; Choi, J.-K.; Lee, J.-H. Design of a Highly Sensitive and Selective C_2H_5OH Sensor Using p-Type Co_3O_4 Nanofiber. *Sens. Actuators, B* **2012**, *161*, 570−577.
(41) Cao, A.; Hu, J.; Liang, H.; Song, W.; Wan, L.; He, X.; Gao, X.; Xia, S. Hierarchically Structured Cobalt Oxide (Co_3O_4): The

Morphology Control and Its Potential in Sensors. *J. Phys. Chem. B* **2006**, *110*, 15858−15863.
(42) Xu, J.; Jia, X.; Lou, X.; Xi, G.; Han, J.; Gao, Q. Selective Detection of HCHO Gas Using Mixed Oxides of Zno/$ZnSnO_3$. *Sens. Actuators, B* **2007**, *120*, 694−699.
(43) Sakai, G.; Matsunaga, N.; Shimanoe, K.; Yamazoe, N. Theory of Gas-Diffusion Controlled Sensitivity for Thin Film Semiconductor Gas Sensor. *Sens. Actuators, B* **2001**, *80*, 125−131.
(44) Wen, Z.; Zhu, L.; Mei, W.; Hu, L.; Li, Y.; Sun, L.; Cai, H.; Ye, Z. Rhombus-Shaped Co_3O_4 Nanorod Arrays for High-Performance Gas Sensor. *Sens. Actuators, B* **2013**, *186*, 172−179.
(45) Hsieh, J.; Liu, C.; Ju, Y. Response Characteristics of Lead Phthalocyanine Gas Sensor: Effects of Film Thickness and Crystal Morphology. *Thin Solid Films* **1998**, *322*, 98.
(46) Seiyama, T.; Kagawa, S. Study on a Detector for Gaseous Components Using Semiconductive Thin Films. *Anal. Chem.* **1966**, *38*, 1069−1073.
(47) Xu, H.; Liu, X.; Cui, D.; Li, M.; Jiang, M. A Novel Method for Improving the Performance of ZnO Gas Sensors. *Sens. Actuators, B* **2006**, *114*, 301−307.
(48) He, T.; Chen, D.; Jiao, X.; Wang, Y.; Duan, Y. Solubility-Controlled Synthesis of High-Quality Co_3O_4 Nanocrystals. *Chem. Mater.* **2005**, *17*, 4023−4030.
(49) Wu, Z.; Jin, R.; Liu, Y.; Wang, H. Ceria Modified MnO_x/TiO_2 As a Superior Catalyst for NO Reduction with NH_3 at Low-Temperature. *Catal. Commun.* **2008**, *9*, 2217−2220.
(50) Kang, M.; Park, E. D.; Kim, J. M.; Yie, J. E. Manganese Oxide Catalysts for NOx Reduction with NH_3 at Low Temperatures. *Appl. Catal., A* **2007**, *327*, 261−269.